

## Architecture of SV40 tubular virus nano-particles from an energy landscape perspective: A computational study

Karim M. ElSawy\*

Department of Chemistry, College of Science, Qassim University, Mulaidah  
52571, Saudi Arabia

Correspondence author: km.elsawy@qu.edu.sa

### Abstract

#### Background

The polymorphic assembly of polyomaviridae capsids into spherical or tubular nano-particles presents a fundamental challenge in understanding viral self-organization.

#### Objectives

Here, we the structural and energetic factors affecting the architecture of non-infectious tubular Simian Virus 40 (SV40) particles, which hold promise for targeted drug delivery.

#### Methodology

By uniquely integrating an atomically detailed model of the energy landscape for VP1 pentamer trimers with viral tiling theory, we successfully predicted the structure of these tubular assemblies.

#### Results

Our predicted tubular particle diameter ( $\sim 424$  Å) is in close agreement with the experimentally observed range of 400-450 Å, and the predicted arrangement of pentamer subunits on the tubular surface closely mirrors cryo-electron microscopy data. A key finding is that the architecture of these tubular structures is largely determined by the lowest energy inter-pentamer packing within the trimer, observed at pH 5. Furthermore, our model predicts a destabilization of tubular structures at pH 8, consistent with experimental observations and suggesting a pH-dependent assembly mechanism.

#### Conclusion

This work provides a crucial mechanistic framework for understanding the physical principles governing capsid polymorphism in polyomaviridae, which can inform the rational design of nano-scale VLPs for nanotechnology and drug delivery.

### Keywords:

Virus assembly, virus assembly polymorphism, Nano-particles, tubular SV40, computer simulation, free energy landscape

## **Introduction**

Virus-like-particles (VLPs) are self-assembling biomolecular structures with a multitude of potential medical uses in drug delivery [1], gene therapy [2] and most notably as vaccines [3-6]. The structural stability and biocompatibility of VLPs make them suitable for drug delivery, with surface functionalization enhancing circulation half-life and target specificity [7]. VLPs can be engineered to deliver therapeutic proteins and RNAs efficiently [8]. They can overcome traditional delivery challenges by enhancing cargo packaging and release, as demonstrated in engineered VLPs (eVLPs) that can achieve high levels of gene editing in various tissues with minimal off-target effects [9].

Simian virus 40 (SV40), a member of the family Polyomaviridae, possesses the potential to serve as a drug or gene delivery vector due to its ability to transduce a broad spectrum of human cells [10], including haematopoietic stem cells [11]. A distinguishing feature of viruses in the Polyomaviridae family is the unusual organisation of their capsid proteins: They occur uniquely in clusters of five, called pentamers, as opposed to the commonly observed mix of 12 pentamers and otherwise hexamers (clusters of six) predicted by Caspar-Klug Theory [12]. In particular, the viral capsid of SV40 is composed of 72 pentamers of the VP1 protein that are arranged with icosahedral symmetry [13]. The unique pentameric arrangement of SV40 capsid proteins could potentially enhance the immunogenicity and stability of VLP-based vaccines [14, 15].

The assembly of the viral capsid of SV40 from its protein building blocks has been studied from both theoretical [12, 16-21] and experimental [22-27] points of view. Experimentally, it has been shown that the recombinant VP1 protein assembles in insect cells into VLPs in the absence of other virion constituents [28], and that such VLPs are morphologically indistinguishable from the wild-type SV40. SV40 is hence a useful system for studying virus disassembly [29]. Interestingly, it has also been shown that the VP1 pentamers self-assemble into a variety of polymorphic aggregates of spherical or tubular particles depending on pH, calcium concentration or ionic strength [30, 31]. While the spherical particles can package the viral genome and are hence infectious, their tubular variants contain little or no DNA [32]. Therefore, the assembly of tubular particles is therapeutically desirable, and a deeper understanding of their assembly could be valuable for targeted drug delivery [33-35].

Mathematical models for the structure and assembly of viral capsids have been investigated over the last few decades [12, 36]. Notably, Caspar-Klug theory [12] has been successful for most viruses except for polyoma and papilloma viruses where it falls short of predicting their capsid structure. A promising approach for solving Caspar-Klug structural puzzles has been initiated by the viral tiling theory (VTT) [17] where the surface lattice of the viral capsid is expressed in terms of pentagonal tessellations. The predictive power of the VTT is significantly enhanced relative to Caspar-Klug theory through its ability to locate not only the location of virus capsid proteins but also through locating protein-protein interactions. Interestingly, VTT has also been able to predict the structure of the tubular variants of the spherical particles [37]. Given the scarcity of structural data for the tubular particles, this gives an invaluable starting point for understanding the assembly of these particles.

In this work, we map the association free energy landscape of three of SV40 VP1 pentamers in order to locate their stable configurations at pH5 and pH8. The topology of the energy landscape is discussed and its implication to higher order sheet structures are highlighted. We then use this knowledge along with the VTT in order to predict the curvature and closure mode of SV40 tubular structure. The relative stability of the constructed tubular structures is then inferred in terms of goodness of closure of the VTT surface tessellation. Finally, the constructed tubular structures are compared to available experimental data.

## Methods

### Computation of the binding free energy landscape

. Based on the assumption that the decision between different final products of assembly is made at the early stages of assembly when, for example for spherical particles, the radius and curvature of the particles are fixed, we choose to focus our analysis on a trimer of pentamers. The trimer is an aggregate formed from 15 VP1 capsid proteins, later referred to as trimers for brevity. Viral Tiling Theory shows that there are three different bonding environments between SV40 trimers in the capsid of SV40 [18], only one of which is capable of supporting formation a tubular structure. Experimental data on the structure of this trimer were extracted from the pdb-files related to the X-ray crystal structure of SV40 [38]. The configurational space this trimer can be represented via the packing angles  $\gamma_1$  and  $\gamma_2$ , that indicate the relative orientations of the pentamers as shown in Figure 1 (b) and serve as collective degrees of freedom.

Intuitively,  $\gamma_1$  and  $\gamma_2$  represent the "hinge angles" or "bending angles" between adjacent VP1 pentamers within the trimer.  $\gamma_1$  describes the angle at which the first and second pentamer are joined, dictating their relative orientation in space. Similarly,  $\gamma_2$  describes the angle at which the second and third pentamer are joined. These two angles are critical because they determine the local curvature and geometry of the pentamer assembly, which ultimately dictates the overall shape (e.g., flat sheet, curved helix, or closed particle) that the larger viral structure can adopt. By systematically varying these angles, we can map out all possible packing arrangements and identify the most energetically favorable ones.

The binding free energy landscape emerges from the variation of binding free energy within this ( $\gamma_1$ ,  $\gamma_2$ ) space. This landscape allows us to study the relative stabilities of the assembled particles. We computed the potential energy surface (PES) of the trimer across a grid in the ( $\gamma_1$ ,  $\gamma_2$ ) space, using a  $5^\circ$  resolution over a range of  $0^\circ$  to  $60^\circ$  for both angles. These limits were chosen to encompass the range of structures observed experimentally. To obtain the atomic coordinates at each grid point, we used rotation around the intersection lines of partial least square regression planes passing through neighboring pentamers. We computed the trimer's PES at two pH values (5.0 and 8.0) by adjusting the protonation states of ionizable residues using the PROPKA algorithm [39, 40]. The CHARMM22 force field [41] was used for calculating the potential energy of the grid structures for each pH value with a relative dielectric constant of 12 used for the electrostatic term, consistent with experimental  $pK_a$  measurement of buried residues [42] and subsequent continuum model calculation of solvation energies [43] in analogous protein systems. To relieve steric clashes arising from the search procedure at the pentamer-pentamer interface, we subjected the system to three consecutive rounds of steepest descent energy minimization. During minimization, backbone atoms were harmonically restrained with an initial force constant of  $30 \text{ kcal mol}^{-1} \text{ \AA}^{-2}$ . The force constant was decreased by  $10 \text{ kcal mol}^{-1} \text{ \AA}^{-2}$  after each round. After this minimization stage the RMSD of the backbone atoms was about  $0.27 \text{ \AA}$  relative to the initial structure. In order to account for the effect of disulfide linkage formation and bound calcium ions, the above minimisation protocol was repeated for possible combinations of 'with/without calcium ions' and 'with/without disulfide linkages'. Presence of a disulfide linkage was determined based on a distance threshold of  $2.05 \pm 0.03 \text{ \AA}$  for the S-S distance of inter-pentamer cystein residues [44]. The positions of the calcium ions were determined based on a maximum distance of  $4.0 \text{ \AA}$  from Glu 216 in one pentamer to Glu 330 for the first binding site and to ASP 345 for the second binding site in neighbouring pentamers [38]. Distance restraints were applied to these distances during the minimization stage described above.

We calculated the binding free energy  $\Delta G_{\text{binding}}$  at each grid point in the ( $\gamma_1$ ,  $\gamma_2$ ) configurational space using the following thermodynamic expression:

$$\Delta G_{\text{binding}} = \Delta G_{\text{trimer}} - (\Delta G_{\text{pentamer 1}} + \Delta G_{\text{pentamer 2}} + \Delta G_{\text{pentamer 3}}) + \Delta E_{\text{vdw}}$$

$$\Delta G = \Delta G_{\text{total.solv}} = \Delta G_{\text{elec}} + \Delta G_{\text{apolar}}$$

The total solvation free energy  $\Delta G_{\text{total.solv}}$  can be expressed as a sum of electrostatic  $\Delta G_{\text{elec}}$  and non polar  $\Delta G_{\text{apolar}}$  components [45]. A finite difference solution of the linearized Poisson-Boltzmann equation was used for calculating the electrostatic component [46] as implemented in the APBS package [47] where a final grid spacing of 0.5 Å was used. The relative dielectric constants of the solvent and protein were set to 78.54 and 12 respectively and the salt concentration was set to 0.15 M. The non-polar component was calculated as a solvent-accessible surface area (SASA) dependant term where each Å<sup>2</sup> of SASA contributes 5.0 cal mol<sup>-1</sup> Å<sup>-2</sup> to the solvation free energy [48]. The change in the van der Waals component of the potential energy  $\Delta E_{\text{vdw}}$  was extracted from the potential energy landscape computed using the CHARMM22 force field [41].

Unlike molecular dynamics simulations [49, 50], which are inherently dependent on time-domain conformational sampling, this study explores the viral assembly process through the binding free energy landscape. Importantly, in the method adopted in this study, the search procedure explicitly defines the limits of the configurational space to be explored and circumvents timescale issues. This approach has been used successfully in studying DNA [51] and protein [52, 53] energy landscapes. Moreover, the topology of the energy landscape, defined in terms of the connectivity of the energy valleys, provides a powerful framework for understanding the formation, transformation or decomposition of transient intermediates during the viral assembly process.

## **Results and discussion**

The interaction of protein subunits within tubular virus nano-particles has been explained by the viral tiling theory where subunit-subunit interaction is reflected in a periodic surface tessellation of pentamers. Such abstraction of protein interaction in terms of tessellation is useful for understanding the formation of virus particles. Correct closure of the tessellation is thereby necessary for particle stability. More specifically, correct closure of the surface tessellation of a flat sheet of protein subunits can, therefore, be viewed as a requirement for the formation of tubular particles. Two key ingredients of this approach are: which type of interaction is appropriate for a correct tessellation of a flat sheet structure, and what is the most favourable way to close this tessellation in order to form the tubular particle. The first of these has been uniquely solved by the viral tiling theory [54] whilst the second is addressed in this manuscript.

### **Topology of the association free energy landscape:**

Three types of subunit interactions are known to exist within polyomaviridae of which only trimer-dimer interaction (Figure 1 c) is predicted by the viral tiling theory to be appropriate for flat sheet structures [54]. The starting point of our calculations was therefore the X-ray structure of the trimer-dimer interaction (three pentamers; 15 protein subunits) of Simian Virus 40 (SV40). The association free energy landscape of the three pentamers was calculated in a 2-dimensional configurational space defined by their packing angles ( $\gamma_1$  &  $\gamma_2$ ; Figure 2). The free energy minima within the energy landscape dictate the stable combinations of these packing angles.

It is noted that the distribution of the energy minima does not conform to a mirror-image symmetry around the diagonal of the energy landscape. The energy minima are only confined to the upper diagonal which indicates that the  $\gamma_1$  packing angle spans a degree of flexibility higher than that of the  $\gamma_2$ . The essence of this topological asymmetry is due to the different pentamer-pentamer interactions within the  $\gamma_1$  and  $\gamma_2$  domains. On the one hand, the  $\gamma_2$  pentamer-pentamer interface involves peptide chains that run back and forward from one

pentamer to the other (Figure 1 c) and therefore imposes steric restraints on  $\gamma_2$  variation. On the other hand, variation of the  $\gamma_1$  is energetically less restricted as it involves mainly two helices whose relative orientation is not hindered by steric restraints (Figure 1 c).

These distinct interaction characteristics are highly sensitive to the local electrostatic environment, which in turn is modulated by pH-induced changes in residue protonation. Specifically, at varying pH values (pH 5.0 and pH 8.0 in this study), the protonation states of ionizable amino acid residues (e.g., aspartate, glutamate, histidine, lysine) at the pentamer-pentamer interfaces are altered. For instance, as pH decreases towards pH 5, carboxyl groups on aspartate and glutamate residues become more protonated (less negatively charged), while amino groups on lysine become more protonated (more positively charged). Conversely, at higher pH values like pH 8, these groups tend to be deprotonated or neutral. Such changes in charge distribution directly affect the strength and nature of electrostatic interactions (attractions and repulsions) between neighboring pentamers. This pH-driven re-tuning of inter-pentamer electrostatic forces profoundly influences the local energy minima within the  $\gamma_1$  and  $\gamma_2$  configurational space, thereby dictating the preferred packing angles and ultimately the macroscopic assembly outcomes.

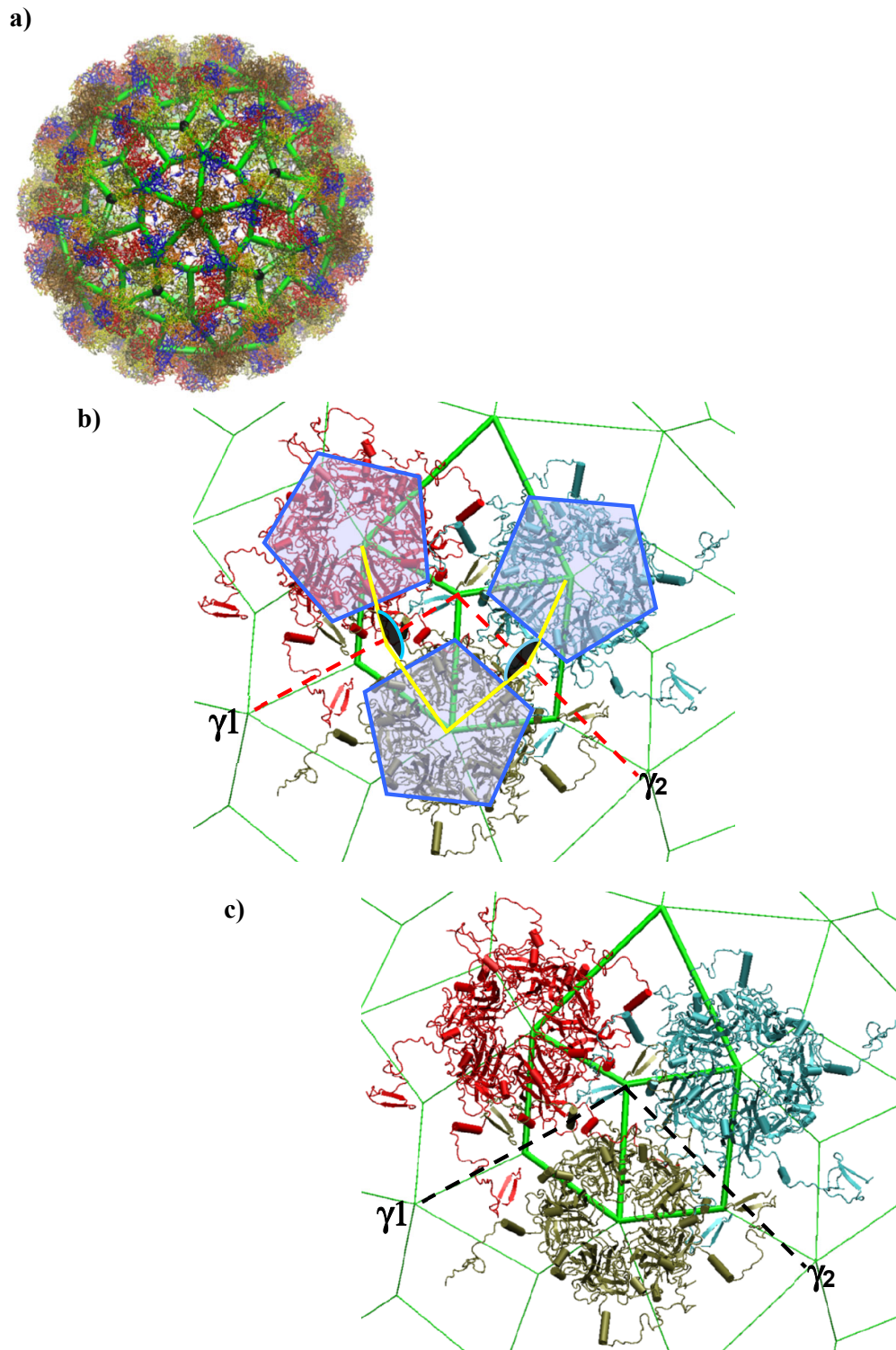


Figure 1. **a)** Tiling of SV40 virus according to the virus tiling theory (VTT). VP1 protein subunits are coloured by chain id in the asymmetric unit cell, the 5-fold symmetry axis is shown as a red sphere while the three-fold axis is shown in black. **b)** Definition of the pentamer-pentamer packing angles ( $\gamma_1$  and  $\gamma_2$ ) within the trimer-dimer interaction environment. **c)** Secondary structure elements of the pentamer-pentamer interface for the  $\gamma_1$  and  $\gamma_2$  domains.

## Implications to the formation of tubular structures

In order to transfer the knowledge gained from the three-pentamer energy landscape to a higher order structure namely a sheet of pentamer aggregates, the  $\gamma_1$  and  $\gamma_2$  of the lowest energy minimum were propagated over a two-pentamer-wide sheet structure (Figure 2 c). Sheet virus structures are aggregates of protein subunits where all pentamer-pentamer packing angles ( $\gamma_1$  and  $\gamma_2$ ) are zero. Interestingly, applying the  $\gamma_1$  and  $\gamma_2$ , corresponding to the lowest energy minimum, i.e. most stable aggregate of the three pentamers, transforms the flat sheet into a helix (Figure 2c) which is reminiscent of the observation of the microtubule growth from gently curved sheets by cryo-electron microscopy [55]. Arise of the helical shape is due to the varying degree of curvature introduced into the flat sheet by the  $\gamma_1$  and  $\gamma_2$  packing angles. Further, the right handedness of the helix is a direct consequence of  $\gamma_2$  being greater than  $\gamma_1$  at the lowest energy minimum. This is in turn due to the topological asymmetry of the association free energy landscape explained previously which means that the values of  $\gamma_1$  and  $\gamma_2$  are not simply interchangeable. The helix radius, pitch and inclination angle of the helix are noticeably dependent on pH and existence/absence of calcium and/or disulphide bridges (Table 1). At pH5 SV40 is known to form tubular structures whose diameter ranges from 400 to 450 Å [56]. Interestingly, in absence of bound calcium ions and disulphide bridges at pH5, the predicted helix diameter (~424 Å) lies within experimental range. However, presence of disulphide bridges and bound calcium ions at pH8 yields also a helical structure whose diameter (~416 Å) lies within that range.

In order to investigate the possibility of emergence of tubular particles from the constructed helices, three helices were interdigitated (Figure 2 d). This resulted in tube like structures with a varying degree of closure of VTT surface tessellation depending on the helix pitch and inclination angle. The goodness of closure was measured by the degree of asymmetry introduced in the tessellation lengths at the helix-helix interface (Table 1). At pH5, in absence of calcium and disulphide bridges the tessellation lengths at the helix-helix interface (86.06, 97.58) Å show less variation than their counterparts at pH8 in absence of calcium and presence of disulphide bridges (80.29, 107.64) Å (Table 1). This indicates that SV40 tubular structures are destabilized at pH8 relative to their counterparts at pH5 which is in agreement with experimental observation of these particles at pH5 [31].

## Comparison with experimental results

Given that the helix-helix interaction is absent from the energetic model used in the calculation of the association free energy landscape, it is desirable to investigate how the surface structure of the tubular particle predicted at pH5 (Figure 2 d) compares to experimental results. The surface structure of the tubular particles of polyoma viruses with a diameter of 400-450 Å has been examined by cryo-electron microscopy [56]. In order to compare this data (Figure 3 A; adapted from Figure 2A in [56]) to the surface structure of the predicted tubular particle (Figure 2 d), a flattened version of that particle (by cutting along the principal axis of the tube) was superposed on Figure 3 a. Despite lack of helix-helix interaction from our energetic model, inspection of Figure 3b reveals that the distribution of the pentamers on the surface of the tubular SV40 particle predicted at pH5 (no calcium, no disulphide bridges) comply reasonably well with that observed experimentally such that the pentamer-pentamer interactions are fairly reproduced. This indicates that the long range structure of SV40 tubular particles is determined to a large extent by local pentamer-pentamer interactions such that it is pretty much dictated by the curvature of the pentamer aggregates at the early stages of the assembly.

While the consistency of our structural predictions with existing cryo-EM data [56] provides a significant validation of our model, we acknowledge that this represents the primary form of experimental comparison at this stage. Future studies employing time-resolved

experimental techniques, such as stopped-flow light scattering or time-resolved cryo-electron microscopy, could provide valuable insights into the kinetics of tubular particle assembly and the formation of potential intermediate structures predicted by our energy landscape analysis. Furthermore, mutagenesis studies targeting key inter-pentamer interfaces identified in our model could experimentally probe the energetic contributions of these interactions to the assembly process and the stability of the resulting tubular structures. Such experiments would provide a more direct and dynamic validation of the mechanistic principles uncovered in this computational study.

The ability to computationally predict and understand the assembly of SV40 tubular nanoparticles opens promising avenues for their application in nanomedicine [57]. The observed pH-dependent stability of these tubular structures, with stability at pH 5 and destabilization at pH 8 (as supported by our model and experimental observations [56], presents a potential trigger mechanism for targeted drug release. Nanoparticles loaded with therapeutic agents could be designed to remain intact under physiological pH conditions (pH ~7.4) during circulation, thus minimizing premature drug release. Upon reaching acidic tumor microenvironments [58] (pH ~6.5-7.0) or upon cellular uptake via endocytosis leading to lower endosomal/lysosomal pH (pH ~5.0-6.0)[59], the destabilization of the tubular structure could be exploited to release the encapsulated drug specifically at the target site. Furthermore, the well-defined and predictable architecture of these viral-like nanoparticles, as revealed by our study, could also be harnessed for vaccine development by presenting specific regulators [21] and antigens[60] on their surface. The insights gained from our energy landscape analysis can guide the rational design and engineering of these nanoparticles for enhanced stability, targeted delivery, and improved therapeutic efficacy

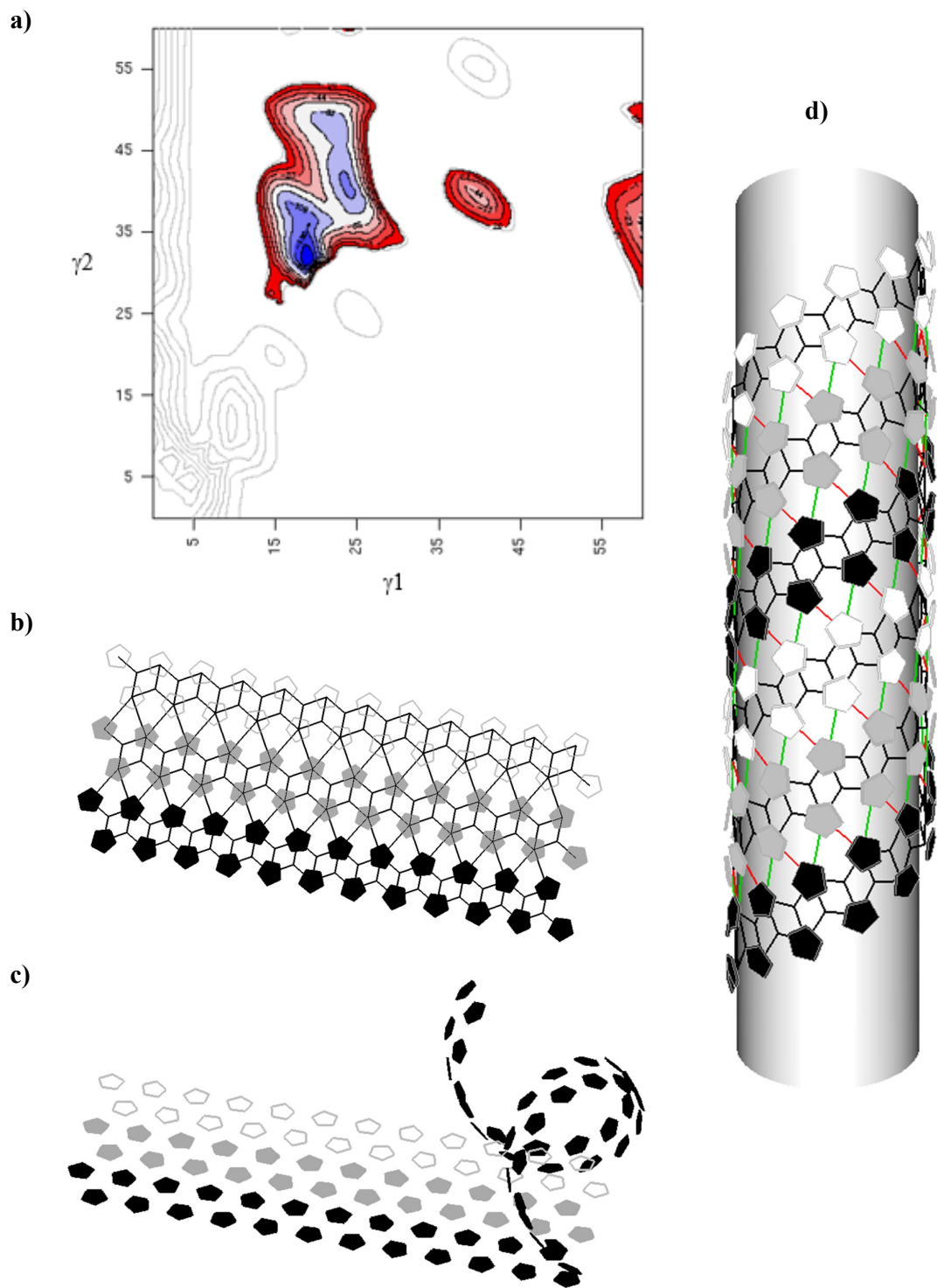


Figure 2 **a)** Contour plot of the association free energy landscape of the three pentamers at 0.15 M NaCl, pH5, no bound Calcium ions and without disulphide bridges. The colour ramp ranges from deep blue (most stable) to dark red (least stable  $\sim -5$  kcal mol<sup>-1</sup>). Contours corresponding to positive binding free energy change (unstable configurations) are shown as grey lines. **b)** Flat sheet structure of aggregate of pentamers with the corresponding tiling shown as black lines. **c)** Emergence of helical structure upon applying  $\gamma_1$  and  $\gamma_2$  of the lowest energy minimum in (a) to the bottom layer of the flat sheet. **d)** Interdigitated helices with the corresponding tiling of the helix-helix interface shown as red ( $\sim 86.1$  Å) and green ( $\sim 97.6$  Å) lines. Tiling within helices is shown as black lines ( $\sim 54.7$  Å).

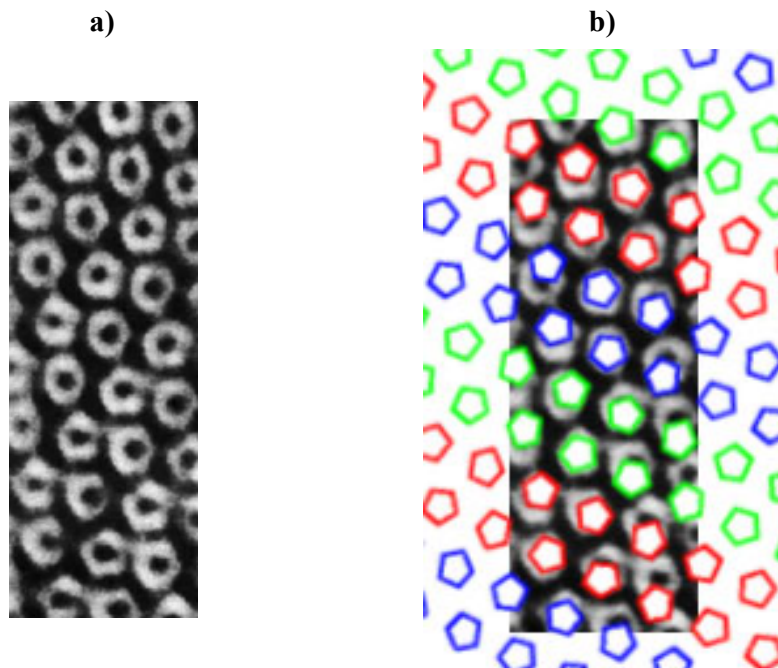


Figure 3 **a)** A filtered cryo-EM image of the front layer of a flattened tubular polyoma virus particle (adapted from Figure 2A in [56]). **b)** A flattened version (shown in colour) of the tubular particle predicted in Figure 2d (by cutting along the tube principal axis) superposed on **(a)**.

**Table 1** The helix parameters and tiling edge lengths corresponding to the  $\gamma_1$  and  $\gamma_2$  packing angles of the lowest energy minima at pH5 and pH8

pH	Calcium	Disulphide bridges	$\gamma_1$	$\gamma_2$	Helix parameters				Lengths of tiling edges			Number of helices /tube
					Hand	Helix pitch	Helix diameter	Inclination angle	Within Helix	Helix-Helix interface		
5	no	no	18.6	31.9	1	535.54	<b>423.66</b>	26.06	54.70±0.77	86.06±0.85	97.58±0.33	3
5	no	yes	19.5	35.1	1	522.50	386.12	28.26	54.40±0.93	79.65±0.02	90.45±0.15	3
5	yes	no	19.1	34.9	1	535.58	388.06	28.80	54.45±0.91	82.88±0.01	92.08±0.17	3
5	yes	yes	19.4	35.2	1	526.60	384.34	28.57	54.40±0.93	81.40±0.01	89.56±0.17	3
8	no	no	19.5	36.3	1	527.46	371.91	29.64	54.31±0.99	81.18±0.09	87.79±0.01	3
8	no	yes	18.6	32.8	1	542.70	<b>412.57</b>	27.23	54.64±0.81	80.29±1.05	107.64±0.39	3
8	yes	no	19.1	34.8	1	538.54	386.39	28.87	54.46±0.91	83.40±0.04	92.98±0.04	3
8	yes	yes	23.5	40.7	1	430.06	342.09	27.47	53.62±1.24	115.46±0.21	120.04±1.26	2

## **Conclusion**

By integrating an atomically detailed energy landscape of VP1 trimers with viral tiling theory, we have successfully predicted the architecture of SV40 tubular particles. The predicted particle diameter ( $\sim 424$  Å) closely matches the experimentally observed range (400–450 Å), and the model accurately reflects the underlying pentamer subunit interactions in relation to their key packing angles. Furthermore, our prediction of tubular structure destabilization at pH 8, contrasting with their stability at pH 5 observed experimentally, underscores the pH-dependent nature of this assembly.

This interdisciplinary approach provides a novel framework for elucidating the structural principles governing viral assembly polymorphism in polyomaviridae. Our findings offer a significant step towards a deeper understanding of the physical determinants of viral assembly polymorphism, with potential implications for controlling VLP morphology for targeted drug delivery and vaccine development, particularly by exploiting pH-sensitive assembly pathways.

The computational model employed allowed us to identify the key packing angles and energetic preferences that govern the local curvature and the overall architecture of the tubular particles. However, we acknowledge that this focus on local interactions does not fully capture the potential influence of longer-range and cooperative effects. Longer-range interactions, such as electrostatic forces between non-adjacent trimers along the tube, could contribute to the overall stability and rigidity of the structure. Cooperative effects, where the binding of one pentamer to a trimer influences the binding of subsequent pentamers, might affect the assembly kinetics and the distribution of tube diameters. To address these limitations in future work, several avenues could be explored. Coarse-grained models could be employed to simulate the assembly of larger tubular structures and capture the collective behavior of multiple trimers. These models would sacrifice some atomic detail but allow for the exploration of longer-range interactions and assembly dynamics. Alternatively, multiscale modeling approaches could be used, combining the atomic-level description of trimer interactions with a coarse-grained representation of the tube. Furthermore, implicit solvent models with anisotropic dielectric properties could better represent the complex electrostatic environment within the assembling tube. Finally, experimental studies, such as time-resolved assembly assays combined with computational modeling, could provide valuable insights into the assembly kinetics and cooperative phenomena.

Further refinement of the model, incorporating the above mentioned limitations such as electrostatic forces between non-adjacent trimers and exploring different kinetic pathways of assembly, could lead to even more accurate predictions and a more complete understanding of the self-assembly process. This study lays a crucial foundation for the rational design and manipulation of viral nanostructures for diverse biomedical applications.

## **Acknowledgement**

The author is deeply grateful to Dr. Reidun Twarock and Dr. Leo Caves, University of York, for their insightful and helpful remarks

## References

1. Georgens, C., J. Weyermann, and A. Zimmer, *Recombinant virus like particles as drug delivery system*. *Curr Pharm Biotechnol*, 2005. **6**(1): p. 49-55.
2. Lehn, P., et al., *Gene delivery systems: Bridging the gap between recombinant viruses and artificial vectors*. *Advanced Drug Delivery Reviews*, 1998. **30**(1-3): p. 5-11.
3. Fakruddin, J.M., et al., *Noninfectious papilloma virus-like particles inhibit HIV-1 replication: implications for immune control of HIV-1 infection by IL-27*. *Blood*, 2007. **109**(5): p. 1841-1849.
4. Yang, L., et al., *A VLP-Based Vaccine Candidate Protects Mice against Japanese Encephalitis Virus Infection*. *Vaccines (Basel)*, 2022. **10**(2).
5. Gupta, R., et al., *Platforms, advances, and technical challenges in virus-like particles-based vaccines*. *Front Immunol*, 2023. **14**: p. 1123805.
6. Adugna, T., et al., *Advancements in nanoparticle-based vaccine development against Japanese encephalitis virus: a systematic review*. *Front Immunol*, 2024. **15**: p. 1505612.
7. Travassos, R., et al., *Tailored Viral-like Particles as Drivers of Medical Breakthroughs*. *Int J Mol Sci*, 2024. **25**(12).
8. Travassos, R., et al. *Tailored Viral-like Particles as Drivers of Medical Breakthroughs*. *International Journal of Molecular Sciences*, 2024. **25**, DOI: 10.3390/ijms25126699.
9. Raguram, A., *Abstract I009: Leveraging engineered virus-like particles for protein and RNA delivery*. *Molecular Cancer Therapeutics*, 2024. **23**(11\_Supplement): p. I009-I009.
10. Gazdar, A.F., J.S. Butel, and M. Carbone, *SV40 and human tumours: myth, association or causality?* *Nat Rev Cancer*, 2002. **2**(12): p. 957-64.
11. Strayer, D.S., *Gene therapy using SV40-derived vectors: what does the future hold?* *J Cell Physiol*, 1999. **181**(3): p. 375-84.
12. Caspar, D.L. and A. Klug, *Physical principles in the construction of regular viruses*. *Cold Spring Harb Symp Quant Biol*, 1962. **27**: p. 1-24.
13. Rayment, I., et al., *Polyoma virus capsid structure at 22.5 Å resolution*. *Nature*, 1982. **295**(5845): p. 110-115.
14. Abdzaid, A.M. and A.S. Jabbar, *Article Review - Virus-Like Particles: A Comprehensive Review of Design, Applications, and Future Directions*. *Stallion Journal for Multidisciplinary Associated Research Studies*, 2024. **3**(3): p. 30-32.
15. Kawano, M., M. Matsui, and H. Handa, *SV40 virus-like particles as an effective delivery system and its application to a vaccine carrier*. *Expert Rev Vaccines*, 2013. **12**(2): p. 199-210.
16. Bruinsma, R.F., et al., *Viral Self-Assembly as a Thermodynamic Process*. *Physical Review Letters*, 2003. **90**(24): p. 248101.
17. Twarock, R., *Mathematical virology: a novel approach to the structure and assembly of viruses*. *Philos Transact A Math Phys Eng Sci*, 2006. **364**(1849): p. 3357-73.
18. Keef, T., A. Taormina, and R. Twarock, *Assembly models for Papovaviridae based on tiling theory*. *Phys Biol*, 2005. **2**(3): p. 175-88.
19. Fejer, S.N., *Minimalistic coarse-grained modeling of viral capsid assembly*. *Prog Mol Biol Transl Sci*, 2020. **170**: p. 405-434.
20. Waltmann, C., et al., *Assembly and Stability of Simian Virus 40 Polymorphs*. *ACS Nano*, 2020. **14**(4): p. 4430-4443.
21. Orłowski, J. and S. Grinstein, *Na<sup>+</sup>/H<sup>+</sup> exchangers*. *Compr Physiol*, 2011. **1**(4): p. 2083-100.

22. Garcea, R.L., *Biologic constraint on modelling virus assembly*. same volume, 2008.
23. Zlotnick, A., et al., *Mechanism of capsid assembly for an icosahedral plant virus*. *Virology*, 2000. **277**(2): p. 450-6.
24. Bertolotti-Ciarlet, A., et al., *Structural requirements for the assembly of Norwalk virus-like particles*. *J Virol*, 2002. **76**(8): p. 4044-55.
25. Jao, C.C., et al., *Cys9, Cys104 and Cys207 of simian virus 40 Vp1 are essential for inter-pentamer disulfide-linkage and stabilization in cell-free lysates*. 1999. **80**(9): p. 2481-2489.
26. van Rosmalen, M.G.M., et al., *Revealing in real-time a multistep assembly mechanism for SV40 virus-like particles*. *Science Advances*. **6**(16): p. eaaz1639.
27. Asor, R., et al., *Effect of ionic strength on the assembly of simian vacuolating virus capsid protein around poly(styrene sulfonate)*. *The European Physical Journal E*, 2023. **46**(11): p. 107.
28. Kosukegawa, A., et al., *Purification and characterization of virus-like particles and pentamers produced by the expression of SV40 capsid proteins in insect cells*. *Biochim Biophys Acta*, 1996. **1290**(1): p. 37-45.
29. Salunke, D.M., D.L. Caspar, and R.L. Garcea, *Self-assembly of purified polyomavirus capsid protein VP1*. *Cell*, 1986. **46**(6): p. 895-904.
30. Salunke, D.M., D.L. Caspar, and R.L. Garcea, *Polymorphism in the assembly of polyomavirus capsid protein VP1*. 1989. **56**(5): p. 887-900.
31. Kanesashi, S.-n., et al., *Simian virus 40 VP1 capsid protein forms polymorphic assemblies in vitro*. *J. Gen. Virol.*, 2003. **84**(7): p. 1899-1905.
32. Lecatsas, G. and O.W. Prozesky, *Excretion of morphological variants of human polyoma virus*. *Archives of Virology*, 1975. **47**(4): p. 393-397.
33. Kiselev, N.A. and A. Klug, *The structure of viruses of the papilloma-polyoma type : V. Tubular variants built of pentamers*. *Journal of Molecular Biology*, 1969. **40**(2): p. 155-157.
34. Aljabali, A.A.A., et al., *The Viral Capsid As Novel Nanomaterials for Drug Delivery*. *Future Science OA*, 2021. **7**(9): p. FSO744.
35. Goldberg, M., R. Langer, and X. Jia, *Nanostructured materials for applications in drug delivery and tissue engineering*. *J Biomater Sci Polym Ed*, 2007. **18**(3): p. 241-68.
36. Toyooka, R., et al., *Explicit description of viral capsid subunit shapes by unfolding dihedrons*. *Communications Biology*, 2024. **7**(1): p. 1509.
37. Keef, T., A. Taormina, and R. Twarock, *Classification of capped tubular viral particles in the family of Papovaviridae*. *J. Phys. Condens. Matter* 2006(14): p. S375.
38. Stehle, T., et al., *The structure of simian virus 40 refined at 3.1 Å resolution*. *Structure*, 1996. **4**(2): p. 165-82.
39. Hui Li, A.D.R.J.H.J., *Very fast empirical prediction and rationalization of protein pKa values*. 2005. **61**(4): p. 704-721.
40. Dolinsky, T.J., et al., *PDB2PQR: expanding and upgrading automated preparation of biomolecular structures for molecular simulations*. *Nucleic Acids Research*, 2007. **35**(suppl 2): p. W522-W525.
41. Brooks, B.R., et al., *CHARMM - a Program for Macromolecular Energy, Minimization, and Dynamics Calculations*. *Journal of Computational Chemistry*, 1983. **4**(2): p. 187-217.
42. Garcia-Moreno, B., et al., *Experimental measurement of the effective dielectric in the hydrophobic core of a protein*. *Biophys Chem*, 1997. **64**(1-3): p. 211-24.
43. Sept, D., N.A. Baker, and J.A. McCammon, *The physical basis of microtubule structure and stability*. 2003. **12**(10): p. 2257-2261.

44. Thomas, E.C., *Disulphide bonds and protein stability*. 1988. **8**(2-3): p. 57-63.
45. Sitkoff, D., K.A. Sharp, and B. Honig, *Accurate Calculation of Hydration Free Energies Using Macroscopic Solvent Models*. *Journal of Physical Chemistry*, 1994. **98**(7): p. 1978-1988.
46. Randolph, E.B. and H. Michael, *A New Paradigm for Parallel Adaptive Meshing Algorithms*. *SIAM J. on Scientific Computing*, 2000. **22**(4): p. 1411-1443.
47. Baker, N.A., et al., *Electrostatics of nanosystems: Application to microtubules and the ribosome*. *Proceedings of the National Academy of Sciences of the United States of America*, 2001. **98**(18): p. 10037-10041.
48. Swanson, J.M., R.H. Henchman, and J.A. McCammon, *Revisiting free energy calculations: a theoretical connection to MM/PBSA and direct calculation of the association free energy*. *Biophys J*, 2004. **86**(1 Pt 1): p. 67-74.
49. Hagan, M.F. and D. Chandler, *Dynamic Pathways for Viral Capsid Assembly*. 2006: p. biophysj.105.076851.
50. Nguyen, H.D., V.S. Reddy, and C.L. Brooks, 3rd, *Deciphering the kinetic mechanism of spontaneous self-assembly of icosahedral capsids*. *Nano Lett*, 2007. **7**(2): p. 338-44.
51. ElSawy, K.M., M.K. Hodgson, and L.S.D. Caves, *The physical determinants of the DNA conformational landscape: an analysis of the potential energy surface of single-strand dinucleotides in the conformational space of duplex DNA*. *Nucleic Acids Research*, 2005(18): p. 5749-5762.
52. Gia G. Maisuradze, D.M.L., *Free energy landscape of a biomolecule in dihedral principal component space: Sampling convergence and correspondence between structures and minima*. 2007. **67**(3): p. 569-578.
53. ElSawy, K.M., *Energy Landscape of Pentapeptides in a Higher-Order Conformational Subspace*. *Advances in Physical Chemistry*, 2016. **2016**: p. doi:10.1155/2016/3240674.
54. Twarock, R., *Mathematical models for tubular structures in the family of Papovaviridae*. *Bull Math Biol*, 2005. **67**(5): p. 973-87.
55. Chretien, D., S.D. Fuller, and E. Karsenti, *Structure of growing microtubule ends: two-dimensional sheets close into tubes at variable rates*. *J. Cell Biol.*, , 1995. **129**(5): p. 1311-1328.
56. Baker, T.S., D.L.D. Caspar, and W.T. Murakami, *Polyoma virus 'hexamer' tubes consist of paired pentamers*. *Nature*, 1983. **303**(5916): p. 446-448.
57. Yan, D., et al., *The application of virus-like particles as vaccines and biological vehicles*. *Appl Microbiol Biotechnol*, 2015. **99**(24): p. 10415-32.
58. Gatenby, R.A., et al., *Acid-mediated tumor invasion: a multidisciplinary study*. *Cancer Res*, 2006. **66**(10): p. 5216-23.
59. Poole, B. and S. Ohkuma, *Effect of weak bases on the intralysosomal pH in mouse peritoneal macrophages*. *J Cell Biol*, 1981. **90**(3): p. 665-9.
60. Campbell, K., et al., *Delivering Two Tumour Antigens Survivin and Mucin-1 on Virus-Like Particles Enhances Anti-Tumour Immune Responses*. *Vaccines (Basel)*, 2021. **9**(5).